BIOPHYSICS

Deformation of microtubules regulates translocation dynamics of kinesin

Syeda Rubaiya Nasrin[1†], Christian Ganser[2†], Seiji Nishikawa[3], Arif Md. Rashedul Kabir[1], Kazuki Sada[1,3], Takefumi Yamashita[4], Mitsunori Ikeguchi[5], Takayuki Uchihashi[2,6], Henry Hess[7], Akira Kakugo[1,3]*

Microtubules, the most rigid components of the cytoskeleton, can be key transduction elements between external forces and the cellular environment. Mechanical forces induce microtubule deformation, which is presumed to be critical for the mechanoregulation of cellular events. However, concrete evidence is lacking. In this work, with high-speed atomic force microscopy, we unravel how microtubule deformation regulates the translocation of the microtubule-associated motor protein kinesin-1, responsible for intracellular transport. Our results show that the microtubule deformation by bending impedes the translocation dynamics of kinesins along them. Molecular dynamics simulation shows that the hindered translocation of kinesins can be attributed to an enhanced affinity of kinesins to the microtubule structural units in microtubules deformed by bending. This study advances our understanding of the role of cytoskeletal components in mechanotransduction.

INTRODUCTION

Living organisms are exposed to exogenous forces such as gravitational, hydrostatic, or mechanical forces as well as endogenous forces caused by their internal physical activities. These forces influence the microenvironment of cells and affect their development and remodeling. Microtubules, the most rigid filamentous protein in the cytoskeleton, are composed of protofilaments of α-tubulin and β-tubulin dimers, and participate in intracellular transport (*1*, *2*). In intracellular transport, the motor proteins kinesin and dynein translocate along the microtubules by consuming energy from adenosine triphosphate (ATP) hydrolysis. The integrity of the microtubule is inevitably essential as it serves as the track for the transport process. In cells, microtubules are known to undergo deformation due to internal and external mechanical forces (*3*–*8*). The mechanical deformation of microtubules is reported to regulate dynein-driven (*9*) and kinesin-driven (*10*) transport. However, how the microtubule deformation regulates transport has been an open question. Lattice defects, caused by the absence of tubulin dimers, in the deformed microtubules (*11*, *12*) have been the major suspect (*13*, *14*). Any direct evidence to confirm the role of microtubule lattice defects is still missing. Molecular-level studies are required to unveil the effect of alterations in the microtubule structure on motor protein-driven transport. In this work, we investigate kinesin translocation along deformed microtubules using high-speed atomic force microscopy (HS-AFM), which offers nanometer spatial resolution and subsecond temporal resolution (*15*–*17*), thereby overcoming limitations of fluorescence microscopy, optical microscopy, and optical tweezers (*18*). Our results show that the motility of kinesin is hindered by the bending of microtubules, even in the absence of deformation-induced lattice defects. We also found the retardation of kinesin translocation to be caused by both tension and compression of microtubules. Even along the central microtubule region where neither compression nor tension is expected, the impeded translocation of kinesin is observed. This regulation of kinesin's motility by microtubule deformation could be attributed to the altered affinity of kinesins to deformed tubulin dimers, which is confirmed by our molecular dynamics (MD) simulation of tubulin-kinesin binding. By investigating the microtubule's interaction with kinesin, we address the critical mechano-responsive role of microtubules in cellular mechanotransduction.

RESULTS

Visualization of microtubules free from lattice defects with HS-AFM

Using HS-AFM, we monitored the movement of single kinesins along microtubules by immobilizing them on a supported lipid bilayer through electrostatic interaction. For this, we prepared the supported lipid bilayer with a thickness of ~4 nm on mica using the vesicle fusion method (fig. S1, A and B) (*19*, *20*). Figure 1A shows an HS-AFM image of a microtubule immobilized on the lipid membrane, as confirmed by the height profile with a microtubule height of ~25 nm (Fig. 1B) (*21*, *22*). The high-resolution observation technique enabled us to detect the protofilaments constituting the microtubules (Fig. 1B). Next, kinesins (40 nM) were applied to the microtubules, and their translocation along the microtubules was initiated by introducing ATP. The average density of kinesin bound to microtubules was 12 kinesins/μm. We used an ATP concentration of 5.0 μM to slow down the translocation and facilitate the tracking of the kinesins along microtubules under HS-AFM (*23*). Bent microtubules, free of lattice defects, were obtained by immobilizing on lipid bilayer islands, which covered the mica substrate discontinuously (figs. S2 and S3). This procedure allowed us to observe the translocation of single kinesins along the bent microtubules in the presence of ATP.

Observation of kinesin translocation along straight and bent microtubules

Figure 1 (C and D) shows the time-lapse HS-AFM images of kinesins translocating along a straight and a bent microtubule, respectively

[1]Faculty of Science, Hokkaido University, Sapporo, Hokkaido 060-0810, Japan. [2]Department of Creative Research, Exploratory Research Center on Life and Living Systems, National Institutes of Natural Sciences, Okazaki, Aichi 444-8787, Japan. [3]Graduate School of Chemical Sciences and Engineering, Hokkaido University, Sapporo, Hokkaido 060-0810, Japan. [4]Laboratory for Systems Biology and Medicine, Research Center for Advanced Science and Technology, The University of Tokyo, Tokyo 153-8904, Japan. [5]Graduate School of Medical Life Science, Yokohama City University, Tsurumi-ku, Yokohama 230-0045, Japan. [6]Department of Physics, Nagoya University, Chikusa-ku, Nagoya 464-8602, Japan. [7]Department of Biomedical Engineering, Columbia University, New York, NY 10027, USA.
*Corresponding author. Email: kakugo@sci.hokudai.ac.jp
†These authors contributed equally to this work.

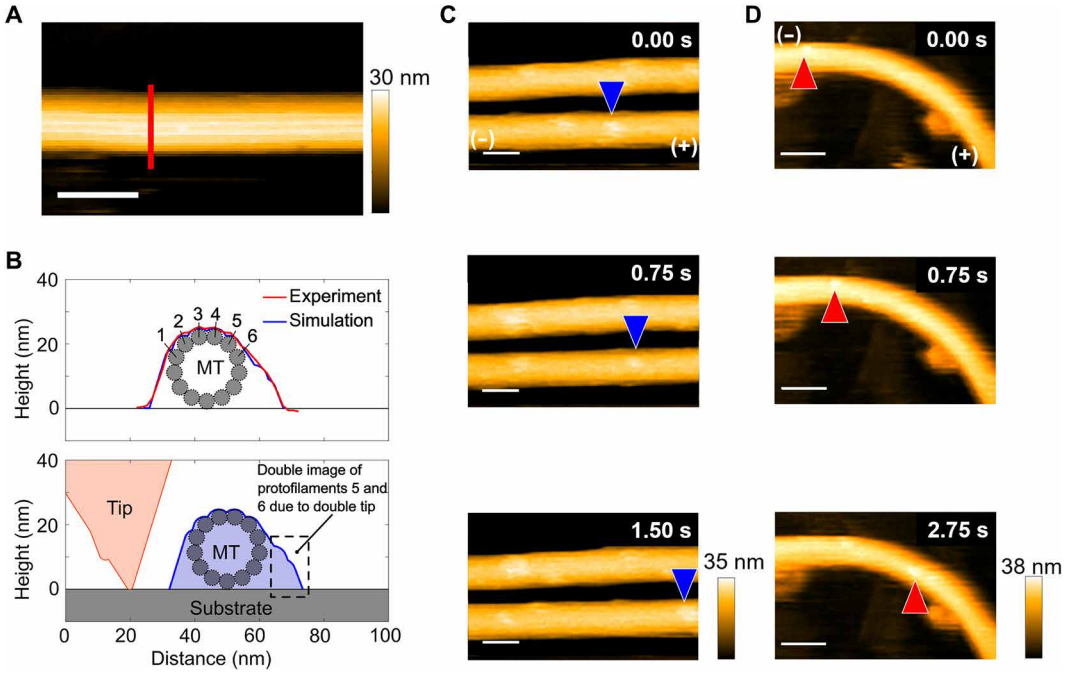

Fig. 1. High-resolution observation of kinesin translocation along microtubules using the HS-AFM. (**A**) HS-AFM image of a straight microtubule on a mica-supported lipid bilayer. Scale bar, 50 nm. The red vertical line is drawn to obtain the height profile of the microtubule. (**B**) The height profile of the microtubule in (A) along the vertical line is shown using the solid red line (top). The height of ~25 nm corresponds to the microtubule diameter. The asymmetry in the line profile can be explained by tip-sample dilation simulation to identify the protofilaments from a line profile of microtubule using a tilted double tip (bottom). From comparing the experimentally obtained line profile of the microtubule with that obtained from the tip-dilation simulation, protofilaments 1 to 6 can be identified by overlapping the measured and simulated line profiles. The two bumps on the right side are caused by the double tip and are ghost images of protofilaments 5 and 6. (**C**) Time-lapse images showing translocation of single kinesin along a straight microtubule. Positions of one kinesin along the microtubule are shown using the blue arrowheads. Plus and minus ends of the microtubule are shown in the first image of the series. Scale bars, 50 nm. The concentrations of ATP and kinesin are 5.0 μM and 40.0 nM, respectively. (**D**) Time-lapse images showing motility of a single kinesin along a bent microtubule. Positions of one kinesin along the microtubule are shown using the red arrowheads. Plus and minus ends of the microtubule are shown in the first image of the series. Scale bars, 50 nm. The concentrations of ATP and kinesin are 5.0 μM and 40.0 nM, respectively.

(movies S1 and S2). The presence of the kinesin on the microtubule protofilaments is confirmed by comparing the height profiles along the longitudinal axis of the microtubule in the presence and absence of kinesins (fig. S4). The mean height of a single kinesin was 3.7 ± 0.1 nm (n = 40) (mean from the Gaussian fit of the distribution of heights ± SE) (fig. S5). Visualization of nonmotile kinesin on microtubules in the presence of adenylyl-imidodiphosphate (AMP-PNP) and single kinesin size analysis confirmed that no kinesin aggregates are observed during imaging (fig. S6A and movie S3). The translocation of kinesins along the protofilaments of the microtubules was confirmed by close monitoring of the kinesins over time (fig. S6B). Taking advantage of the high spatial resolution offered by the HS-AFM, we considered three regions, namely, region 1, region 2, and region 3, along the microtubules' longitudinal axis (Fig. 2A). For bent microtubules, regions 1 and 3 were subjected to tension and compression, respectively (Fig. 2B). The trajectories of the kinesins shown in Figure 2 (C and D) reveal that kinesins consistently translocate along a protofilament without shifting to a neighbor protofilament (*24*). However, the presence of a few nonparallel trajectories suggests that the sidestepping of kinesins is also possible, as reported by the sidestepping probability of 0.13 to 0.18 (*24*, *25*).

We calculated the instantaneous velocities of kinesins from their displacements between every two consecutive frames (Fig. 3A). Comparing regions 1, 2, and 3, no significant differences in the mean instantaneous velocities of kinesins were found for either straight or bent microtubules (Fig. 3B; see also table S1). However, when comparing the respective regions between straight and bent microtubules, the mean instantaneous kinesin velocity was always lower along the bent microtubule (Fig. 3B). It is to mention here that the presence of 40 nM kinesin and 5.0 μM ATP did not cause any gliding of the microtubules on the lipid bilayer (fig. S6C and movie S4), consistent with the previous report (*26*).

The mean instantaneous velocity of the kinesins along a straight microtubule was 83 ± 3 nm/s (mean ± SE, n = 54) (Fig. 4A), which is similar to the previous reports of kinesin velocity in the presence of 5.0 μM ATP (*27*, *28*). The mean instantaneous velocity of kinesins moving along the bent microtubule (Fig. 4A; see also table S2) was 42 ± 3 nm/s (mean ± SE, n = 57), which is significantly lower than that along straight microtubules (t test, $P < 0.0001$). We initially hypothesized that the reduced mean instantaneous velocity of kinesins along the bent microtubules occurs because of increased pausing events when compared to the case of straight microtubules (Fig. 4B). Therefore, we analyzed the pausing events to obtain kinesin pause frequencies while translocating along the microtubule (fig. S7A; see also table S3). The pause frequencies between the straight and bent microtubules did not differ statistically significantly (Mann-Whitney test, P = 0.36). The instantaneous translocation velocity of kinesins without considering the pauses did not significantly differ from that

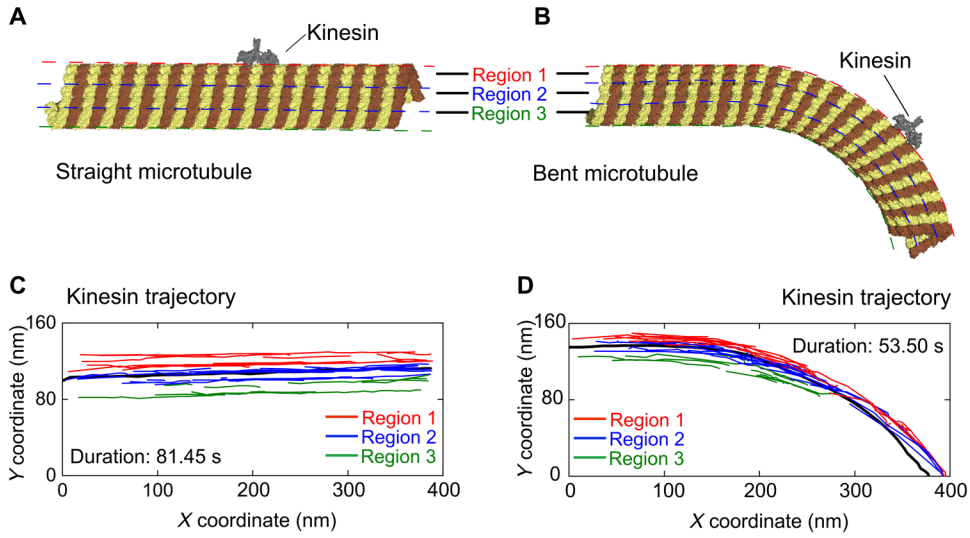

Fig. 2. Deformation of a microtubule by bending. (**A**) Cartoon showing a straight microtubule with a kinesin attached. Three longitudinal regions are considered along the microtubule: region 1, region 2, and region 3, respectively. Region 2 in the middle of the straight microtubule is considered to be along the two protofilaments in the middle, and the two protofilaments over and below this region are considered as regions 1 and 3, respectively. (**B**) Cartoon showing the deformation of protofilaments in a bent microtubule with a kinesin attached. As a result of bending, the protofilaments in region 1 are stretched, while those in region 3 are under compression. Region 2 in between regions 1 and 3 is presumed to have experienced flexural stress. (**C**) Trajectories of kinesins moving along the straight microtubule recorded for 81.45 s. Kinesin trajectories along regions 1, 2, and 3 are represented using red, blue, and green lines, respectively. (**D**) Trajectories of kinesins moving along the bent microtubule recorded for 53.50 s. Kinesin trajectories along regions 1, 2, and 3 are represented using red, blue, and green lines, respectively. Only the kinesin trajectories that could distinctly be assigned to one of the three regions on the microtubules were considered in (C) and (D).

with pauses (fig. S7B; see also table S4). However, the slowing down of the kinesins does not involve the presence of any lattice defect in microtubules, such as missing tubulin dimers (*14*), because HS-AFM can directly detect these defects (*29*) (fig. S8, A and B, and movie S5) and we did not observe defects in the analyzed microtubules. We also attempted to observe kinesin translocation along microtubules having defects, defined as one or more missing tubulin dimers (fig. S8C and movie S6). The threshold to detect these missing tubulin dimers is the presence of a depression or hole in the microtubule lattice, which is significantly deeper than the microtubule's surface roughness. We determined that kinesin stops in front of a defect and detaches from the microtubule after 1.1 ± 0.8 s (mean ± SD, n = 20).

Microtubule curvature–dependent behavior of kinesin translocation

To further explore the effect of microtubule deformation on the translocation behavior of kinesins, we investigated the correlation between the curvature (κ) of the bent microtubule and the mean instantaneous velocity of kinesins. The mean instantaneous velocity of the kinesins along the bent microtubules was found to be strongly dependent on the curvature of the microtubules (Fig. 5 and fig. S9A). A gradual decrease in the instantaneous velocities of kinesins was observed at curvatures higher than 1 μm^{-1} (Fig. 5), similar to what was reported previously (*9*). The mean instantaneous velocity of kinesin at low curvature region ($\kappa \leq 1\ \mu m^{-1}$) of the microtubules was 97 ± 3 nm/s (mean ± SE; fig. S9B), which was significantly higher than that (34 ± 2 nm/s; mean ± SE) observed at the high curvature region ($\kappa > 1\ \mu m^{-1}$) of the microtubules (fig. S9C). If the kinesin velocity is modeled as inversely dependent on the sum of the time for ATP binding (66 ms at 5.0 μM ATP) and the time required to complete the chemomechanical cycle, which is assumed to increase with curvature exponentially ($18\ ms \times e^{\left(\frac{\kappa}{\kappa_c}\right)}$) (time constants calculated from velocities at 5.0 mM, i.e., at saturating concentration and at 5.0 μM ATP) to reflect a first-order linear approximation of the effect of the curvature on the activation energy of the rate-limiting step, the data in Figure 5 can be fitted with a characteristic curvature, $\kappa_c = 4.0\ \mu m^{-1}$. The same observation holds true for the cases of other bent microtubules, proving the reproducibility of the curvature-dependent kinetics of kinesin translocation (fig. S10).

Our observation from the HS-AFM agreed to what we observe using the total internal reflection fluorescence (TIRF) microscopy technique (figs. S11 and S12 and movie S7). We prepared single kinesins labeled with quantum dot (*30*) and observed their motility along fluorescent dye–labeled microtubules in the presence of 1 mM ATP (fig. S11A). The mean instantaneous velocity of kinesin along undeformed microtubules, 762 ± 44 nm/s (n = 16), agreed with literature (*27*) (fig. S11B). We found that with increasing curvature of the microtubule segments, the mean translocation velocities of quantum dot–labeled kinesins decreased similar to the HS-AFM observation with fitting to the relation between mean instantaneous velocities of kinesins and microtubule curvatures (fig. S12).

The effect of microtubule deformation on kinesin binding affinity

The effect of microtubule deformation on the binding affinity of kinesins to the microtubules was evaluated by calculating the binding rate constant k_{on}, the dissociation rate constant k_{off}, and the apparent dissociation constant K_d (Table 1). k_{on} is given by the number of kinesins bound on the microtubule in a unit of kinesin concentration, microtubule length, and time ($M^{-1}\ \mu m^{-1}\ s^{-1}$) (*31*, *32*). The significantly higher value of k_{on} of kinesins on bent microtubule compared to straight microtubule indicates that the kinesins bind at a faster

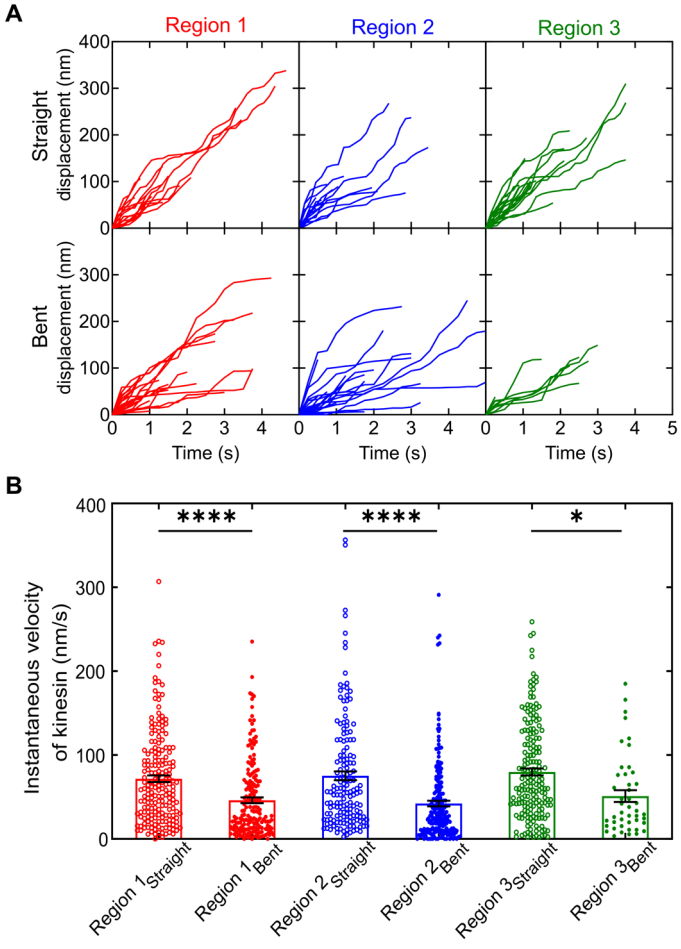

Fig. 3. Comparison of kinesin translocation dynamics along a straight and bent microtubule. (**A**) Time-displacement profile of kinesins moving along region 1 (red), region 2 (blue), and region 3 (green) of the straight microtubule (top) and the bent microtubule (bottom). (**B**) Comparison of mean instantaneous velocities of kinesins translocating along the three different regions along the straight and bent microtubules along with the distributions of the data. The instantaneous velocities of kinesins along regions 1, 2, and 3 of the straight microtubule are shown using red, blue, and green open circles, respectively, and those along the bent microtubule are shown using solid circles. The instantaneous velocities of kinesins along the three regions of the straight and bent microtubules were not normally distributed. Statistical significance of the differences among the mean instantaneous velocities was tested by the Kruskal-Wallis test followed by the Dunn's multiple comparisons test. ****$P < 0.0001$ and *$P < 0.05$. Error bar, SE (see also table S1).

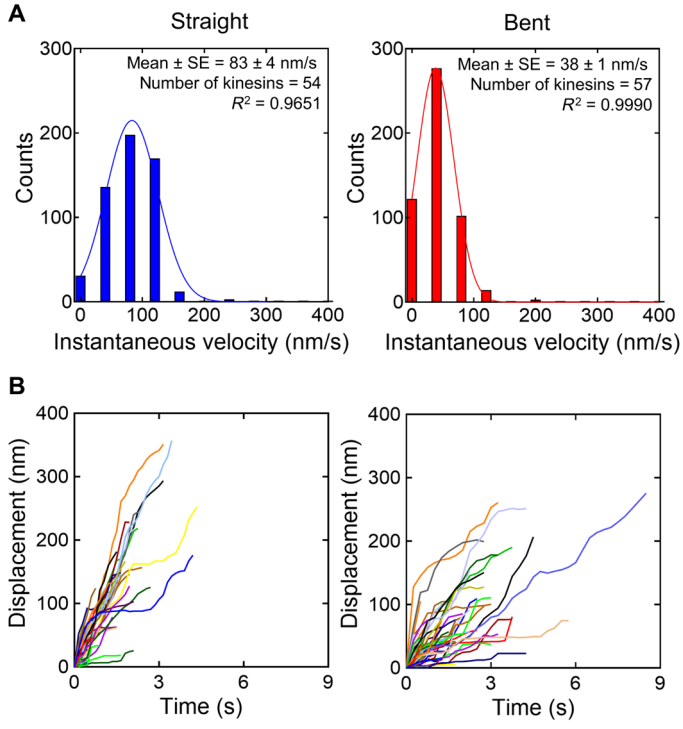

Fig. 4. Comparison of mean instantaneous velocities of kinesin along straight and bent microtubules. (**A**) Distribution of instantaneous velocities of the kinesins translocating along the straight (left) and bent (right) microtubules shown in Figure 2 (C and D). Number of instantaneous velocities considered for the plots are 549 and 517, respectively. Counts of frames where the kinesin velocities were the same were bin-separated. The events were normally distributed and were fitted to the Gaussian equation for normal distribution $y = y_o + \frac{A}{w\sqrt{\frac{\pi}{2}}} e^{-2\frac{(x-x_c)^2}{w^2}}$, where A, w, and x_c are areas, widths, and centers of the peak with y-offset equal to zero (0), respectively. Mean velocities from the fits with SEs, the number of kinesins tracked, and the goodness of fits (R^2) are provided in the legends of the graphs. The mean instantaneous velocities obtained from the distributions are significantly different (unpaired t test for normally distributed data, $P < 0.0001$) (see also table S2). (**B**) Time-displacement plots of representative kinesins along straight (left) and bent (right) microtubules. Analysis of kinesins traveling along one straight microtubule and one bent microtubule is included in this plot. The numbers of kinesin molecules traced for the analysis were 54 and 57 for straight and bent microtubules shown in Figure 2 (C and D, respectively).

rate to bent microtubules than to the straight ones. Kinesins also spent longer time (1.64 ± 0.17 s; mean ± SE, $n = 57$) on the bent microtubule compared to the straight microtubule (1.04 ± 0.13 s; mean ± SE, $n = 57$) (fig. S13; see also table S5). Thus, the mechanical deformation of microtubules is found to prolong the binding time of kinesins to microtubules (*33*). As a result, k_{off}, the reciprocal of the binding time, was higher for straight microtubules than for bent microtubules.

MD simulations of the effect of the microtubule deformation on the kinesin-tubulin interactions

To investigate the mechanism from the energetic aspect by which the mechanical deformation of microtubule influences the interaction between the kinesin and tubulin, we performed all-atom MD simulations of the protein complex system consisting of a tubulin dimer and a motor domain of kinesin (*34*) [Protein Data Bank (PDB) ID: 4LNU; Fig. 6A] solvated by 0.15 M saline (see Materials and Methods for details). Here, the kinesin is in the apo state, while α-tubulin and β-tubulin bind to guanosine-5′-triphosphate (GTP) and guanosine-5′-diphosphate (GDP), respectively. Using MD simulations, we calculated the interaction energy between kinesin and tubulin deformed by tension, compression, or flexure. The interaction energy is the sum of the Coulomb interaction energy and Lennard-Jones interaction energy acting between tubulin dimer and kinesin. We averaged the Coulomb interaction energy and Lennard-Jones interaction energy over all the structures sampled by the MD simulation (*35*–*37*).

The molecular-level deformation in the bent microtubule was described as the change of inter-tubulin distance restrained by the environment. This external restraint was modeled by a harmonic

bias potential (fig. S14A) $U(r) = \frac{1}{2}k(r - r_e)^2$. Here, r is the center-of-mass (COM) distance between α-tubulin and β-tubulin, k is the spring constant, and r_e is its target value, which was set to be between 4.1 and 4.5 nm with a 0.1-nm interval. For each r_e value, five MD simulations were conducted independently. The COM distance between α-tubulin and β-tubulin measured through x-ray crystallography is 4.22 nm in the kinesin-tubulin complex provided in PDB ID: 4LNU. Therefore, the COM distances lower and higher than 4.22 nm will refer to the compression and tension in the tubulin dimers, respectively. Note that the difference of 0.1 nm in α-tubulin and β-tubulin COM distance in the MD simulations corresponds to microtubule bending with curvature of ≤2.0 μm^{-1}. Figure 6B shows the overlaid structures of the complexes with α-tubulin and β-tubulin COM distances equal to 4.1, 4.2, and 4.3 nm. We found that the interaction between tubulin and kinesin motor domain at different inter-tubulin distances resulted in the variation in the three-dimensional positions of the tubulin monomers, relative to each other (Fig. 6, C to E). We observed that the interaction energy between α-tubulin and β-tubulin in a dimer decreased with increased tension on the dimer (fig. S14B). The interaction energy between tubulin dimer and kinesin motor domain varied significantly in the cases where the tubulin dimer underwent deformations, either compression or tension (Fig. 7A and fig. S14C). The interaction energy is a dominant part of the binding enthalpy despite the effect of the desolvation energy, and the binding affinity is determined from the binding enthalpy and binding entropy. Thus, the binding affinity between tubulin dimer and kinesin under compression/tension conditions may be discussed on the basis of interaction energy. The increased interaction energy would indicate the decrease of the dissociation rate, which is consistent with our experimental finding, where we see the decreased instantaneous kinesin velocity during translocation along the deformed microtubule. We also found that the change in Coulomb's interaction energy is more pronounced than that of the Lennard-Jones interaction, which means that the tension or compression of the microtubule may increase ionic or hydrogen bonds.

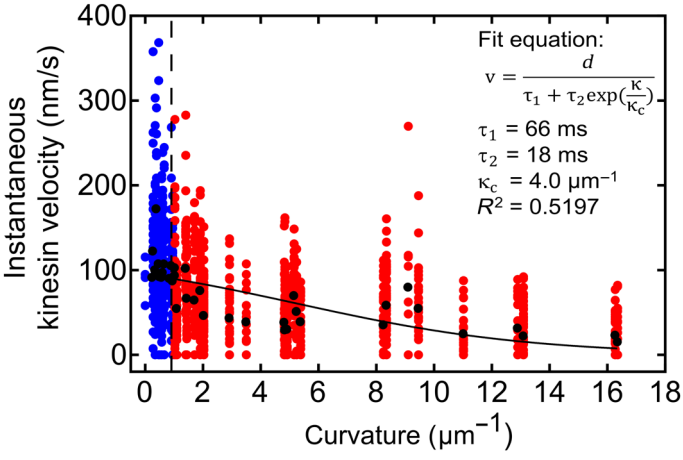

Fig. 5. Kinesin instantaneous velocities along different curvatures of a deformed microtubule. Curvature-dependent translocation velocity of kinesin along the bent microtubule shown in Figure 1D. Blue and red colors are used to identify the low and high curvature regions of the bent microtubule. The number of kinesins considered is 37. It should be noted that this number is different from that in Figure 4 because only kinesins moving from the low to high curvature regions along the microtubule were considered for this analysis. The total number of instantaneous velocities is 1567. The vertical dashed line at the curvature (κ) of 1 μm^{-1} represents a critical curvature reported in (*9*). We fitted the mean velocities versus curvature plot to the equation $v = \frac{d}{\tau_1 + \tau_2 \exp(\frac{\kappa}{\kappa_c})}$; here, d = 8 nm is the kinesin step size, τ_1 = 66 ms is the time for ATP binding at 5.0 μM ATP, and $\tau_2 = \left(18\ ms \times \exp(\frac{\kappa}{\kappa_c})\right)$ is the time required to complete the chemomechanical cycle, which is assumed to increase exponentially with a characteristic curvature, κ_c = 4.0 μm^{-1} (as a first approximation of the effect of the curvature on the activation energy of the rate-limiting step). The time constants are calculated from the velocities at saturating (5.0 mM) and 5.0 μM ATP concentrations at zero curvature, and the characteristic curvature, κ_c, is the only fit parameter. The dotted lines represent the SE of the regression line.

In the bent microtubule, the tubulin dimer is slightly deformed not only by compression or tension but also by angular stress (region 2 in Fig. 2B). To mimic the angular deformation, we introduced an additional restraint on the distance between the COM of N-side domain (R2-K164) of α-tubulin and the COM of β-tubulin (Fig. 6E and fig. S15A). This distance was restrained at 4.1, 4.2, and 4.3 nm, while α-tubulin and β-tubulin COM distance was restrained to 4.2 nm. It is important to note that the average distance between the N-side domain (R2-K164) of α-tubulin and β-tubulin is around 4.12 nm when the additional restraint is not introduced. With an increased distance between the N-side domain of α-tubulin and β-tubulin, the kinesin-tubulin interaction energy is greatly enhanced (Fig. 7B and fig. S15B). The kinesin-tubulin interaction energy is also sensitive to the angular deformation so that a subtle deformation is expected to slow down the kinesin walk.

DISCUSSION

Using the advantages of HS-AFM in high-resolution imaging, we have shown that compression, tension, or bending of microtubule lattice can significantly slow down the translocation kinetics of kinesins along microtubules. Because kinesin movement slows on all three regions of the bent microtubule (Fig. 3B), the bending deformation of the tubulin, which creates an angle between the two lateral surfaces, appears to have the primary effect. Thus, deformations due to not only compression or tension but also flexural stress have detrimental effect on the kinesin translocation dynamics. The presence of lattice defects on the deformed microtubules is found not to be a requirement in this mechanoregulation of kinesin's translocation. This result is consistent with the precise 8-nm step size of kinesin (*38*), which is also the length of a tubulin dimer. It

Table 1. Summary of the kinetic parameters. k_{on}, k_{off}, and K_d of kinesin binding to the straight and bent microtubules. The values are mean ± SE (see also data S4).

Microtubule feature	k_{on} ($M^{-1}\ \mu m^{-1}\ s^{-1}$)	k_{off} (s^{-1})	K_d (M μm)
Straight	39,026 ± 32	0.96 ± 0.12	(2.46 ± 0.31) × 10^{-5}
Bent	59,801 ± 186	0.61 ± 0.07	(1.02 ± 0.11) × 10^{-5}

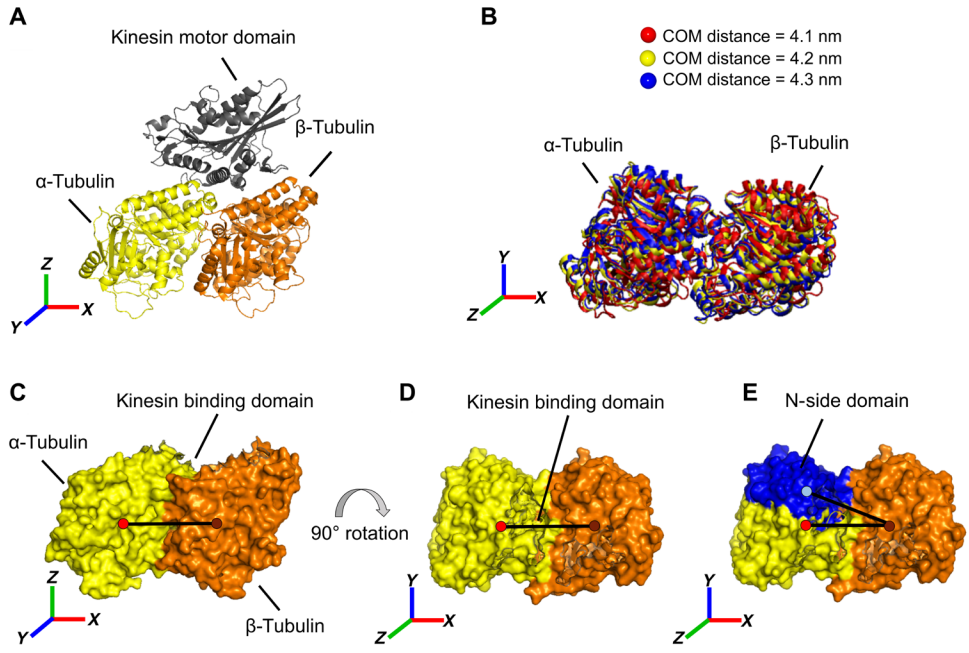

Fig. 6. Replication of microtubule deformation in MD simulation. (**A**) Native tubulin-kinesin complex (PDB ID: 4LNU). α-Tubulin, β-tubulin, and kinesin motor domain are shown in yellow, orange, and gray, respectively. (**B**) Overlaid structures of the tubulin dimers with different tubulin-tubulin COM distances after the formation of complexes with kinesin motor domain. The tubulin dimers with tubulin-tubulin distances of 4.1, 4.2, and 4.3 nm are shown in blue, yellow, and red, respectively. (**C**) The α-tubulin and β-tubulin COM distance is shown by the black line connecting the COMs of the tubulins (PDB ID: 4LNU). The COM distances of α-tubulin and β-tubulin were restrained to 4.1, 4.2, 4.3, 4.4, and 4.5 nm to mimic the compression or tension on the microtubule. Without the restraint, the COM distance between α-tubulin and β-tubulin is 4.2 nm. (**D**) Tubulin dimer in (C) rotated 90°. (**E**) N-side domain (Arg^2 to Lys^{164}) of α-tubulin in blue. An additional harmonic restraint to the COM distance of the N-side domain of α-tubulin and β-tubulin is set to 4.1, 4.2, and 4.3 nm. The COM distance between α-tubulin and β-tubulin is fixed at 4.2 nm. Without the restraint, the COM distance between the N-side domain of α-tubulin and β-tubulin is 4.12 nm.

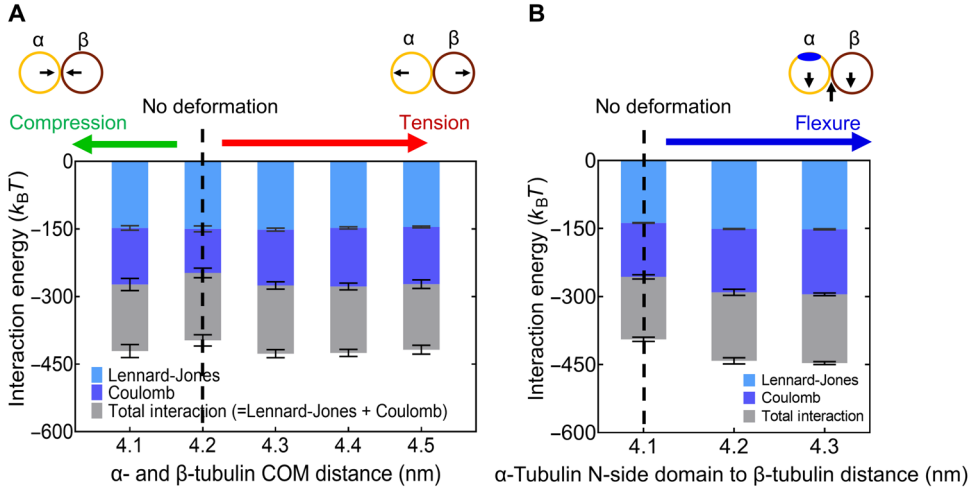

Fig. 7. Elucidation of the kinesin-tubulin interaction dynamics by MD simulations. (**A**) Total interaction energies due to compression and tension on microtubule shown using gray bars are the sums of Coulomb's interaction energy and Lennard-Jones interaction energy. The total interaction energy is altered if the tubulin-tubulin distance is deformed mainly due to the alteration in the Coulomb's interaction between kinesin and tubulin monomers (dark blue bars). The Lennard-Jones interaction energies between kinesin and tubulin dimers remained almost unaffected because of the change in tubulin-tubulin distances (light blue bars). The vertical dashed line represents the inter-tubulin distance equal to that found in the crystal (PDB ID: 4LNU). COM distances of α-tubulin and β-tubulin lower and higher than that referred to tubulin dimer under compression and tension, respectively. Error bar, SE. (**B**) Total interaction energies due to flexural strain on microtubule shown using gray bars are the sums of Coulomb's interaction energy and Lennard-Jones interaction energy. The Coulomb's interaction energy and the Lennard-Jones interaction energy are shown as dark blue bars and light blue bars, respectively. The vertical dashed line represents the inter-tubulin distance equal to that found in the crystal and should correspond to the energy calculated along the vertical dashed line in (A).

demonstrates that defects on the tubulin dimer level do not allow the kinesin to translocate along microtubules. Thus, a decrease in the instantaneous velocity of kinesins is ascribed solely to the deformation of the microtubule, even in the absence of any lattice defect. Our observation of the significant difference in kinesin instantaneous velocities without considering pausing events along straight and bent microtubules relates to a mechanism associated with the kinetics of kinesin binding to the microtubules as highlighted by the altered k_{off}, k_{on}, and apparent K_d values. The apparent K_d values reflect a higher binding affinity of kinesins for bent microtubules than for straight microtubules and indicates stronger intermolecular interactions between the kinesin and tubulins of the bent microtubules. The deformation slows the ATP hydrolysis cycle, significantly increasing the time required to complete the cycle after ATP has bound. A linear approximation of the relationship between the change in the activation energy of the rate-limiting step and the curvature ($\Delta E_A = \kappa_c^{-1} \times \kappa$) yields a characteristic curvature κ_c of 4.0 μm^{-1}. At this curvature, the activation energy of the rate-limiting step is increased by 1 k_BT, which is of a plausible magnitude considering that the 8-nm-long tubulin dimer is noticeably deformed with the lateral surfaces now at an angle of 1.8°. One may consider the possibility of enhanced kinesin-tubulin interaction in bent microtubules to deform the ATP-binding pocket through an allosteric effect. As a result, a decrease in the ATP hydrolysis rate with consequent slowing down of the kinesin motion may take place. Our MD simulations show that a 0.1-nm increase or decrease in the α-tubulin and β-tubulin COM distance, analogous to the tension or compression of the microtubule, causes an increase in the intermolecular interactions between the tubulin dimer and the kinesin motor domain. An increase in this interaction energy is also observed when an angular deformation of the microtubule is replicated in the MD simulation. Because increased interactions lead to slower detachment, this finding is consistent with the experimentally observed decrease in kinesin instantaneous velocity along deformed microtubules. As a result, the alteration in binding affinity of kinesins to deformed microtubules appears as a plausible means to account for the regulated translocation of kinesins.

Our work offers evidence that microtubules can serve as a mechanosensor and can help to understand how microtubules regulate intracellular transport in adverse environments by absorbing mechanical forces (*39*). In general, the findings presented here offer fundamental insights into microtubules' mechanoregulation abilities of cellular events. Our study can also help to understand the role of mechanical forces in regulating interactions between a microtubule and its associated proteins. For example, KLP10A, a member of the kinesin-13 family, is reported to be noncatalytic when bound to the microtubule lattice but becomes catalytic when bound to curved tubulin (*40*). There is also evidence of increased affinity of tumor overexpressing gene domains to curved microtubules (*41*), stable and ordered complex formation by kinesin-13, and curved tubulin protofilaments (*42*–*44*). All these studies emphasize motor-induced microtubule depolymerization, whereas the present work not only clarifies how the affinity between kinesin-1 and microtubules is altered upon microtubule deformation but also demonstrates how this altered affinity regulates intracellular transport. Mice with amyotrophic lateral sclerosis symptoms exhibit a twofold decrease in axonal transport velocity (*45*), demonstrating how the impairment in axonal transport can correlate with disease states in vivo and motivating further research into the underlying mechanisms. A change in the interaction energy between microtubules and its associated motor protein by deformation of microtubules may offer itself as the starting point to an understanding of how microtubules serve as mechanotransducers in cells as exemplified by the above studies (*46*, *47*).

MATERIALS AND METHODS

Purification of tubulin and polymerization to microtubules

Tubulin was purified from fresh porcine brain using a high-concentration Pipes buffer (1 M Pipes, 20 mM EGTA, 10 mM $MgCl_2$; pH adjusted to 6.8 using KOH) (*48*) and stored at −80°C. The tubulin was polymerized into microtubules in the presence of 4 mM GTP at 37°C for 30 min. Then, 1.0 mM paclitaxel was added and again incubated for 15 min at 37°C. The paclitaxel-stabilized microtubules (tubulin concentration = 1.12 μM) were then suspended in a buffer with the composition of 80 mM Pipes (pH 6.9), 2 mM $MgCl_2$, 1 mM EGTA, 1 mM GTP, 50 μM paclitaxel, and 2.74 M glycerol (20 volume %).

Expression and purification of kinesin

A kinesin-1 construct consisting of human kinesin (residues 1 to 465), an N-terminal histidine tag, and a C-terminal Avi-tag was expressed according to the literature (*49*).

Preparation of mica-supported lipid bilayer

Lipid bilayers were prepared using charge neutral lipid 1,2-dipalmitoyl-sn-glycerol-3-phosphocholine (DPPC) and positively charged lipid 1,2-dipalmitoyl-3-trimethylammonium-propane (DPTAP) (Avanti Polar Lipids, Alabaster, AL) having phase transition temperatures 41.3°C (*50*) and ~42.0°C (*51*). A previously published method for the preparation of lipid bilayers was followed (*19*) and is outlined here. Solutions of DPPC and DPTAP in chloroform were mixed at a gravimetric ratio of 3:7. The phase transition temperature of the DPPC and DPTAP lipid bilayer at this composition is around 50°C (*51*). The chloroform was evaporated under a stream of nitrogen gas. The chosen ratio of DPPC to DPTAP was found to be optimal to successfully immobilize microtubules on the lipid bilayer through electrostatic interactions. Then, Milli-Q H_2O was added to obtain a lipid solution (0.5 mg/ml). A mica disk was glued to a cylindrical sample stage with a diameter of 2 mm and cleaved directly before lipid application. A lipid solution (0.5 mg/ml) was added to the mica and incubated for 10 min. The sample stage was then washed thoroughly with imaging buffer [80 mM Pipes (pH 6.9 with KOH), 2 mM $MgCl_2$, and 1 mM EGTA in Milli-Q water]. A stable lipid bilayer on the mica substrate was obtained. To bend microtubules, inhomogeneities in a usually uniform lipid bilayer are necessary to act as pinning sites for the microtubules. Such pinning sites can be holes in the lipid bilayer, second layer lipid islands, or even contaminants of unknown origin (fig. S2A). Microtubules appear to be fixed in place at such pinning sites and can maintain flexibility at the free end (fig. S2B). This flexibility allows the microtubules to adapt a bent conformation, if the free end can be caught by a pinning site (fig. S2, C and D). Pinning sites can be created in several ways. One is to let the lipid dry out and rehydrate. In this case, holes are created, but a large amount of contaminations are also stuck to the lipid surface. A second method is to wash the lipid with the imaging buffer heated to at least 80°C. In this case, holes dominate the surface and contaminations are reduced compared with the first method. A

combination of drying and washing with heated buffer solution was used as it creates a large variety of pinning sites.

Single kinesin translocation assay along microtubule

Two microliters of 1.12 μM paclitaxel-stabilized microtubule solution was placed on the mica-supported lipid bilayer (with or without tris-HCl washing) and left to adsorb on the surface for 10 min. After that, the sample stage was thoroughly washed with 20.0 to 40.0 μl of imaging buffer. Next, a solution of Avi-tag kinesin (600 nM) diluted in buffer composed of 80 mM Pipes, 40 mM NaCl, 1 mM EGTA, 1 mM $MgCl_2$, 20 μM casein, 1 mM dithiothreitol (DTT), and 10 mM paclitaxel (pH 6.8) was applied and allowed to stand for 5 min. For observation of the single kinesins moving along the microtubules, a mixture of kinesin and ATP solution was added with the imaging buffer. The final concentrations of kinesin and ATP during imaging were 40 nM and 5.0 μM, respectively. We used the seemingly high concentration of kinesin because of the small observation area in our observation system. All experiments were carried out at 25°C.

Imaging with high-speed AFM apparatus

The measurements were performed using a laboratory-built HS-AFM (*52*). The topography images were recorded in tapping mode. BL-AC10DS-A2 (Olympus, Tokyo, Japan) cantilevers were used. The cantilevers were about 9 μm long, 2 μm wide, and 130 nm thick with a spring constant of ~0.1 Nm^{-1}, according to the supplier. All images were recorded in the above-specified imaging buffer, where the cantilevers' resonance frequencies were between 400 and 500 kHz. The free oscillation amplitude of the cantilever was set to about 1.5 nm, with a set-point of approximately 80% of the free amplitude during scanning. The carbon tip at the end of the cantilever was grown using electron beam deposition and sharpened using a plasma etcher to a tip radius between 2 and 5 nm. The imaging rate was set to 150 and 250 ms per frame for capturing movies with straight and bent microtubules, respectively. The AFM images were analyzed using laboratory-made analysis software FalconViewer based on Igor Pro 8 and Fiji 1.53c (National Institutes of Health, USA) (*53*).

Preparation of fluorescent dye–labeled microtubules and quantum dot–labeled single kinesin for TIRF observation

We obtained ATTO 565 fluorescent dye–labeled tubulin following a standard protocol (*54*). Microtubules were polymerized from 56 μM tubulin (80% ATTO 565–labeled tubulin and 20% nonlabeled tubulin) in BRB80 [80 mM Pipes, 1 mM $MgCl_2$, and 1 mM EGTA (pH 6.8)] in the presence of 5 mM GTP, 20 mM $MgCl_2$, and 25% dimethyl sulfoxide at 37°C for 30 min. Microtubules were stabilized using taxol buffer (50 μM paclitaxel in BRB80). We used the streptavidin-conjugated quantum dot 525 (Q10143MP, Invitrogen, USA) to label single Avi-tag kinesins through the streptavidin-biotin interaction. The quantum dots were mixed with kinesins at a molar concentration ratio of 1:1 (*30*). According to (*30*), more than 70% of the quantum dots have no kinesins and about 30% of quantum dots have one kinesin attached at this mixing ratio. The percentage of quantum dots with two or more kinesins is less than 10%. The kinesin–quantum dot solution was diluted using the motility buffer [5 μM ATP, casein (3 mg/ml), 20 mM DTT, 40 μM paclitaxel, and anti-fading agents: glucose (9 mg/ml), glucose oxidase (100 U/ml), and catalase (100 U/ml) in BRB80] just before applying it to the flow cell (*55*). The applied concentrations of quantum dot and kinesin were 4 nM, and that of ATP was 1 mM.

Quantum dot–labeled single kinesin translocation assay for TIRF observation

Solutions of DPPC and DPTAP in chloroform were mixed at a gravimetric ratio of 3:7. The chloroform was evaporated under a stream of nitrogen gas. Then, Milli-Q H_2O was added to obtain a lipid solution of 1.0 mg/ml. The lipid mixture prepared was diluted 40 times with 5 mM $MgCl_2$ and sonicated for 10 min before use. A flow cell was prepared by making a narrow channel using double-sided tape on a 28 mm × 50 mm glass slide covered with an 18 mm × 18 mm coverslip. The double-sided tape served as a spacer. The narrow channel was exposed to air plasma for 4 min (10 Pa, 8 mA) in a plasma etcher (SEDE-GE; Meiwafosis Co. Ltd.). The flow cell was coated by applying 20 μl of the lipid mixture and incubating at 50°C for 10 min. The flow cell was washed three times with room temperature BRB80. Next, 10 μl of paclitaxel-stabilized ATTO 565–labeled microtubules diluted 60 times using taxol buffer was introduced to the flow cell and incubated for 10 min. A solution consisting of casein (645 μg/ml), 130 μM DTT, and 13 μM paclitaxel in BRB80 (solution A) was used to wash the flow cell. Bovine serum albumin (1 mg/ml) was applied and incubated for 5 min to prevent nonspecific absorption of kinesins on the substrate. After washing the flow cell with solution A, quantum dot–labeled kinesins in the presence of 1 mM ATP were introduced. The flow cell was observed immediately after the addition of ATP. All experiments were performed at 25°C.

Observation with TIRF microscope

Samples were illuminated with a 15-mW Nikon Ti 3 laser source and visualized using a two-color TIRF microscope (Eclipse Ti2; Nikon) equipped with an oil-coupled Plan Apo 60 × 1.40 objective (Nikon). The 488-nm (30% intensity) and 561-nm (0.5% intensity) lines of the Nikon Ti 3 laser were used to excite quantum dots and the ATTO 565–labeled microtubules, respectively. Images were captured using a cooled complementary metal-oxide semiconductor (CMOS) camera (Neo CMOS; Andor) connected to a PC. The observation of the quantum dot assay was performed by capturing images with an exposure time of 100 ms for quantum dot–labeled kinesins and 30 ms for ATTO 565–labeled microtubules without delay in-between frames. The overall fps (frame per second) of the captured movies was 0.48. The fluorescence images were analyzed by NIS-Elements AR (version 5.30.02, Nikon) and Fiji 1.53c (*53*).

Estimation of parameters

The instantaneous velocities of the kinesins were calculated from the displacement difference of a kinesin between successive frames divided by the time interval. This means "x" number of instantaneous velocities analyzed for the calculation is obtained from considering "$x + 1$" number of frames. A custom-written GNU Octave code was used to determine the curvature of the segments of the bent microtubule (see Supplementary Text and fig. S16). For pause analysis, we calculated the distances traveled by kinesins between every two consecutive frames. When this distance was zero (0), we counted it as one pausing event by the kinesin in the course of translocation along microtubules. To obtain the pause frequencies, we counted the number of pauses and normalized them by dividing with the traveled distances for each kinesin translocating along microtubules. We fitted the distributions of the pausing events to single exponential decay function to obtain mean pause frequencies of 6.08 ± 0.87 μm^{-1} (mean ± SE, n = 57) and 6.01 ± 1.01 μm^{-1} (mean ± SE, n = 57) for the cases of straight and bent microtubules, respectively (fig. S7A).

The mean instantaneous velocities of the kinesins, including and excluding zero velocities, were determined from fitting the distributions of the instantaneous velocities along straight and the bent microtubule to the Gaussian equation for normal distribution (Fig. 4A and fig. S7B). The means from the fit with SEs are reported. The mean run length of quantum dot–labeled kinesins was obtained from bin-independent cumulative probability distributions of the run lengths. The distributions were fitted to the function $y = 1 - e^{\left(\frac{d-d_0}{\tau}\right)}$, where d_0 is the shortest run length measured during analysis; the only fit parameter, the decay constant, τ, gave the mean run length in the distribution (fig. S11A). The mean instantaneous velocities of quantum dot–labeled kinesins in the presence of 1 mM ATP were determined from fitting the distributions of the instantaneous velocities along straight microtubules to the Gaussian equation for normal distribution (fig. S11B). The means from the fit with SEs are reported. The values of k_{on} on straight or bent microtubules were calculated as the number of bound kinesins ($N_{kinesin}$) normalized by kinesin concentration ($C_{kinesin}$), length of the microtubule ($L_{microtubule}$), and observation time (t), i.e., $k_{on} = \frac{N_{kinesin}}{C_{kinesin} \times L_{microtubule} \times t}$. Binding events of kinesins were counted during 81.45 and 53.50 s along straight and bent microtubules, respectively. The lengths of the microtubules were measured from the HS-AFM images using the Fiji software. k_{off} was calculated as the reciprocal of mean binding time. The binding time was defined by the duration of time starting from attachment of the kinesins to microtubule until they were detached from the microtubule, or the imaging was finished. The apparent dissociation constant is defined as $K_d = \frac{k_{on}}{k_{off}}$. Errors were calculated by using the error propagation formula. The distribution of the binding times along straight and bent microtubules did not pass the normality test (D'Agostino and Pearson test and Shapiro-Wilk test). Therefore, we determined the mean binding time from bin-independent cumulative probability distributions of the binding times. The distributions were fitted to the function $y = 1 - e^{\frac{t_0-t}{\tau}}$, where t_0 is the shortest binding time measured during analysis; the only fit parameter, the decay constant, τ, gave the mean binding time in the distribution (fig. S13). The Y axis is the cumulative probability that the kinesin is bound for less than the time on the X axis. Data presented in Figs. 2 to 4 and figs. S7 and S13 are from the same set of kinesins moving along the straight and bent microtubules in Figure 2 (C and D) and movies S1 and S2, respectively. In Figure 5, kinesins that translocate from the low to the high curvature regions of the bent microtubule in Figure 2D are considered.

Statistical analysis

Statistical analyses were performed with GraphPad Prism 8.4.3. A two-tailed Student's t test was used to compare two groups of normally distributed data. One-way ANOVA, followed by Tukey's multiple comparison test, was used to compare among three or more groups of normally distributed data. The Kruskal-Wallis test followed by Dunn's multiple comparison test was used to compare among three or more groups of nonnormal data. The values for the number of events N, the P value, and the specific statistical test performed for each experiment are included in the appropriate figure legend or main text.

MD simulation methods

The structures of the kinesin motor domain and the αβ-tubulin heterodimer of the microtubule used in our MD simulations were taken from the PDB (PDB ID: 4LNU). In this complex, the kinesin motor domain is in the apo-state. The MD simulations were carried out using GROMACS 4.6 (*56*) with the FUJI force field (*57*) and the TIP3P model for protein and water, respectively. After DARPIN was removed, unmeasured hydrogen atoms, 63,575 water molecules, and 0.15 M Na^+ and Cl^- ions were added to the crystal structure. The energy minimization was performed by using the l-BFGS method. The water and ions were equilibrated for 300 ps at 298 K and 1 bar with the heavy atoms of proteins restrained. The whole system was equilibrated for 600 ns under the same conditions. To mimic the effect of the mechanical deformation of microtubules, the COM distances of α-tubulin and β-tubulin were restrained in the product run. Here, a harmonic potential with the spring constant of 4000 kJ mol^{-1} nm^{-2} was used to restrain the distance between α-tubulin and β-tubulin. The minimal distance of the harmonic potential was set to 4.1, 4.2, 4.3, 4.4, and 4.5 nm in respective windows. In each window, five MD simulations were conducted for 210 ns at 298 K and 1 bar. In all MD simulations, the Nose-Hoover coupling and Berendsen coupling to control the temperature and pressure were used, respectively. The time step was set to 3 fs, and all chemical bonds were constrained using the LINear Constraint Solver (LINCS) algorithm. The long-range electrostatic interaction was calculated by using the PME algorithm. The coordinates were sampled every 5000 steps. For each window, we analyzed the interaction energy between tubulins and kinesin. The interaction energy was calculated as the summation of Lennard-Jones interaction and the Coulomb's interaction and averaged over the last 150 ns (*37*). This method of averaging the interaction energies over all the structures sampled by the MD simulation is often used in drug design software to evaluate the affinity between molecules with a low computational cost (*35*, *36*).

To investigate the angular distortion along region 2 (in Fig. 2B) of bent microtubule, we introduced an additional harmonic restraint to the distance between the COM of the N-side domain of α-tubulin and the COM of β-tubulin. Here, the N-side domain consists of 163 residues (Arg^2 to Lys^{164}), and the spring constant was set to 4000 kJ mol^{-1} nm^{-2}. The minimum distance of the harmonic potential was set to 4.1, 4.2, and 4.3 nm, while that for the COM-COM distance between α-tubulin and β-tubulin was 4.2 nm. Without the restraint, the distance between the N-side domain of α-tubulin and β-tubulin was distributed around 4.1 nm. For each restraint condition, five MD simulations were performed for 150 ns.

SUPPLEMENTARY MATERIALS

Supplementary material for this article is available at https://science.org/doi/10.1126/sciadv.abf2211

View/request a protocol for this paper from *Bio-protocol*.

REFERENCES AND NOTES

1. Z. Hejnowicz, A. Rusin, T. Rusin, Tensile tissue stress affects the orientation of cortical microtubules in the epidermis of sunflower hypocotyl. *J. Plant Growth Regul.* **19**, 31–44 (2000).
2. D. Tremblay, L. Andrzejewski, A. Leclerc, A. E. Pelling, Actin and microtubules play distinct roles in governing the anisotropic deformation of cell nuclei in response to substrate strain. *Cytoskeleton* **70**, 837–848 (2013).
3. C. P. Brangwynne, F. C. MacKintosh, D. A. Weitz, Force fluctuations and polymerization dynamics of intracellular microtubules. *Proc. Natl. Acad. Sci. U.S.A.* **104**, 16128–16133 (2007).
4. C. P. Brangwynne, F. C. MacKintosh, S. Kumar, N. A. Geisse, J. Talbot, L. Mahadevan, K. K. Parker, D. E. Ingber, D. A. Weitz, Microtubules can bear enhanced compressive loads in living cells because of lateral reinforcement. *J. Cell Biol.* **173**, 733–741 (2006).
5. G. Steinberg, R. Wedlich-Söldner, M. Brill, I. Schulz, Microtubules in the fungal pathogen Ustilago maydis are highly dynamic and determine cell polarity. *J. Cell Sci.* **114**, 609–622 (2001).

6. A. Straube, G. Hause, G. Fink, G. Steinberg, Conventional kinesin mediates microtubule–microtubule interactions in vivo. *Mol. Biol. Cell* **17**, 907–916 (2006).
7. A. D. Bicek, E. Tüzel, A. Demtochouk, M. Uppalapati, W. O. Hancock, D. M. Kroll, D. J. Odde, Anterograde microtubule transport drives microtubule bending in LLC-PK1 epithelial cells. *Mol. Biol. Cell* **20**, 2943–2953 (2009).
8. J. Wu, G. Misra, R. J. Russell, A. J. C. Ladd, T. P. Lele, R. B. Dickinson, Effects of dynein on microtubule mechanics and centrosome positioning. *Mol. Biol. Cell* **22**, 4834–4841 (2011).
9. S. R. Nasrin, T. Afrin, A. M. R. Kabir, D. Inoue, T. Torisawa, K. Oiwa, K. Sada, A. Kakugo, Regulation of biomolecular-motor-driven cargo transport by microtubules under mechanical stress. *ACS Appl. Bio Mater.* **3**, 1875–1883 (2020).
10. W. W. Ahmed, T. A. Saif, Active transport of vesicles in neurons is modulated by mechanical tension. *Sci. Rep.* **4**, 4481 (2014).
11. C. M. Waterman-Storer, E. D. Salmon, Actomyosin-based retrograde flow of microtubules in the lamella of migrating epithelial cells influences microtubule dynamic instability and turnover and is associated with microtubule breakage and treadmilling. *J. Cell Biol.* **139**, 417–434 (1997).
12. L. Schaedel, S. Triclin, D. Chrétien, A. Abrieu, C. Aumeier, J. Gaillard, L. Blanchoin, M. Théry, K. John, Lattice defects induce microtubule self-renewal. *Nat. Phys.* **15**, 830–838 (2019).
13. M. W. Gramlich, L. Conway, W. H. Liang, J. A. Labastide, S. J. King, J. Xu, J. L. Ross, Single molecule investigation of kinesin-1 motility using engineered microtubule defects. *Sci. Rep.* **7**, 44290 (2017).
14. W. H. Liang, Q. Li, K. M. Rifat Faysal, S. J. King, A. Gopinathan, J. Xu, Microtubule defects influence kinesin-based transport in vitro. *Biophys. J.* **110**, 2229–2240 (2016).
15. T. Ando, T. Uchihashi, T. Fukuma, High-speed atomic force microscopy for nano-visualization of dynamic biomolecular processes. *Prog. Surf. Sci.* **83**, 337–437 (2008).
16. T. Ando, T. Uchihashi, N. Kodera, High-speed AFM and applications to biomolecular systems. *Annu. Rev. Biophys.* **42**, 393–414 (2013).
17. T. Ando, High-speed atomic force microscopy and its future prospects. *Biophys. Rev.* **10**, 285–292 (2018).
18. T. Cordes, S. A. Blum, Opportunities and challenges in single-molecule and single-particle fluorescence microscopy for mechanistic studies of chemical reactions. *Nat. Chem.* **5**, 993–999 (2013).
19. D. Yamamoto, T. Uchihashi, N. Kodera, H. Yamashita, S. Nishikori, T. Ogura, M. Shibata, T. Ando, *Methods in Enzymology* (Elsevier Inc., ed. 1, 2010), vol. 475, pp. 541–564.
20. S. J. Attwood, Y. Choi, Z. Leonenko, Preparation of DOPC and DPPC supported planar lipid bilayers for atomic force microscopy and atomic force spectroscopy. *Int. J. Mol. Sci.* **14**, 3514–3539 (2013).
21. L. A. Amos, T. S. Baker, The three-dimensional structure of tubulin protofilaments. *Nature* **279**, 607–612 (1979).
22. E. Nogales, M. Whittaker, R. A. Milligan, K. H. Downing, High-resolution model of the microtubule. *Cell* **96**, 79–88 (1999).
23. K. J. Bohm, R. Stracke, E. Unger, Speeding up kinesin-driven microtubule gliding in vitro by variation of cofactor composition and physicochemical parameters. *Cell Biol. Int.* **24**, 335–341 (2000).
24. I. A. T. Schaap, C. Carrasco, P. J. De Pablo, C. F. Schmidt, Kinesin walks the line: Single motors observed by atomic force microscopy. *Biophys. J.* **100**, 2450–2456 (2011).
25. S. L. Reck-Peterson, A. Yildiz, A. P. Carter, A. Gennerich, N. Zhang, R. D. Vale, Single-molecule analysis of dynein processivity and stepping behavior. *Cell* **126**, 335–348 (2006).
26. R. Grover, J. Fischer, F. W. Schwarz, W. J. Walter, P. Schwille, S. Diez, Transport efficiency of membrane-anchored kinesin-1 motors depends on motor density and diffusivity. *Proc. Natl. Acad. Sci. U.S.A.* **113**, E7185–E7193 (2016).
27. M. J. Schnitzer, S. M. Block, Kinesin hydrolyses one ATP per 8-nm step. *Nature* **388**, 386–390 (1997).
28. S. Verbrugge, S. M. J. L. Van Den Wildenberg, E. J. G. Peterman, Novel ways to determine kinesin-1's run length and randomness using fluorescence microscopy. *Biophys. J.* **97**, 2287–2294 (2009).
29. C. Ganser, T. Uchihashi, Microtubule self-healing and defect creation investigated by in-line force measurements during high-speed atomic force microscopy imaging. *Nanoscale* **11**, 125–135 (2019).
30. A. Seitz, T. Surrey, Processive movement of single kinesins on crowded microtubules visualized using quantum dots. *EMBO J.* **25**, 267–277 (2006).
31. Y. Shibafuji, A. Nakamura, T. Uchihashi, N. Sugimoto, S. Fukuda, H. Watanabe, M. Samejima, T. Ando, H. Noji, A. Koivula, K. Igarashi, R. Iino, Single-molecule imaging analysis of elementary reaction steps of trichoderma reesei cellobiohydrolase i (Cel7A) hydrolyzing crystalline cellulose Iα and IIII. *J. Biol. Chem.* **289**, 14056–14065 (2014).
32. A. Nakamura, T. Tasaki, Y. Okuni, C. Song, K. Murata, T. Kozai, M. Hara, H. Sugimoto, K. Suzuki, T. Watanabe, T. Uchihashi, H. Noji, R. Iino, Rate constants, processivity, and productive binding ratio of chitinase A revealed by single-molecule analysis. *Phys. Chem. Chem. Phys.* **20**, 3010–3018 (2018).
33. R. A. Cross, A. McAinsh, Prime movers: The mechanochemistry of mitotic kinesins. *Nat. Rev. Mol. Cell Biol.* **15**, 257–271 (2014).
34. L. Cao, W. Wang, Q. Jiang, C. Wang, M. Knossow, B. Gigant, The structure of apo-kinesin bound to tubulin links the nucleotide cycle to movement. *Nat. Commun.* **5**, 5364 (2014).
35. C. L. Verlinde, W. G. Hol, Structure-based drug design: Progress, results and challenges. *Structure* **2**, 577–587 (1994).
36. T. Jain, B. Jayaram, An all atom energy based computational protocol for predicting binding affinities of protein-ligand complexes. *FEBS Lett.* **579**, 6659–6666 (2005).
37. T. Yamashita, E. Mizohata, S. Nagatoishi, T. Watanabe, M. Nakakido, H. Iwanari, Y. Mochizuki, T. Nakayama, Y. Kado, Y. Yokota, H. Matsumura, T. Kawamura, T. Kodama, T. Hamakubo, T. Inoue, H. Fujitani, K. Tsumoto, Affinity improvement of a cancer-targeted antibody through alanine-induced adjustment of antigen-antibody interface. *Structure* **27**, 519–527.e5 (2019).
38. D. L. Coy, M. Wagenbach, J. Howard, Kinesin takes one 8-nm step for each ATP that it hydrolyzes. *J. Biol. Chem.* **274**, 3667–3671 (1999).
39. O. Hamant, D. Inoue, D. Bouchez, J. Dumais, E. Mjolsness, Are microtubules tension sensors? *Nat. Commun.* **10**, 2360 (2019).
40. M. P. M. H. Benoit, A. B. Asenjo, H. Sosa, Cryo-EM reveals the structural basis of microtubule depolymerization by kinesin-13s. *Nat. Commun.* **9**, 1662 (2018).
41. P. Ayaz, X. Ye, P. Huddleston, C. A. Brautigam, L. M. Rice, A TOG:αβ-tubulin complex structure reveals conformation-based mechanisms for a microtubule polymerase. *Science* **337**, 857–860 (2012).
42. C. A. Moores, M. Yu, J. Guo, C. Beraud, R. Sakowicz, R. A. Milligan, A mechanism for microtubule depolymerization by KinI kinesins. *Mol. Cell* **9**, 903–909 (2002).
43. D. Tan, W. J. Rice, H. Sosa, Structure of the kinesin13-microtubule ring complex. *Structure* **16**, 1732–1739 (2008).
44. A. B. Asenjo, C. Chatterjee, D. Tan, V. DePaoli, W. J. Rice, R. Diaz-avalos, M. Silvestry, H. Sosa, Structural model for tubulin recognition and deformation by kinesin-13 microtubule depolymerases. *Cell Rep.* **3**, 759–768 (2013).
45. L. G. Bilsland, E. Sahai, G. Kelly, M. Golding, L. Greensmith, G. Schiavo, Deficits in axonal transport precede ALS symptoms in vivo. *Proc. Natl. Acad. Sci. U.S.A.* **107**, 20523–20528 (2010).
46. A. L. Parker, M. Kavallaris, J. A. McCarroll, Microtubules and their role in cellular stress in cancer. *Front. Oncol.* **4**, 153 (2014).
47. N. Wang, J. P. Butler, D. E. Ingber, Mechanotransduction across the cell surface and through the cytoskeleton. *Science* **260**, 1124–1127 (1993).
48. M. Castoldi, A. V. Popov, Purification of brain tubulin through two cycles of polymerization-depolymerization in a high-molarity buffer. *Protein Expr. Purif.* **32**, 83–88 (2003).
49. K. Fujimoto, M. Kitamura, M. Yokokawa, I. Kanno, H. Kotera, R. Yokokawa, Colocalization of quantum dots by reactive molecules carried by motor proteins on polarized microtubule arrays. *ACS Nano* **7**, 447–455 (2013).
50. R. L. Biltonen, D. Lichtenberg, The use of differential scanning calorimetry as a tool to characterize liposome preparations. *Chem. Phys. Lipids* **64**, 129–142 (1993).
51. A.-L. Troutier, L. Véron, T. Delair, C. Pichot, C. Ladavière, New insights into self-organization of a model lipid mixture and quantification of its adsorption on spherical polymer particles. *Langmuir* **21**, 9901–9910 (2005).
52. T. Ando, N. Kodera, E. Takai, D. Maruyama, K. Saito, A. Toda, A high-speed atomic force microscope for studying biological macromolecules. *Proc. Natl. Acad. Sci. U.S.A.* **98**, 12468–12472 (2001).
53. J. Schindelin, I. Arganda-Carreras, E. Frise, V. Kaynig, M. Longair, T. Pietzsch, S. Preibisch, C. Rueden, S. Saalfeld, B. Schmid, J.-Y. Tinevez, D. J. White, V. Hartenstein, K. Eliceiri, P. Tomancak, A. Cardona, Fiji: An open-source platform for biological-image analysis. *Nat. Methods* **9**, 676–682 (2012).
54. J. Peloquin, Y. Komarova, G. Borisy, Conjugation of fluorophores to tubulin. *Nat. Methods* **2**, 299–303 (2005).
55. S. R. Nasrin, A. M. R. Kabir, K. Sada, A. Kakugo, Effect of microtubule immobilization by glutaraldehyde on kinesin-driven cargo transport. *Polym. J.* **52**, 655–660 (2020).
56. B. Hess, C. Kutzner, D. Van Der Spoel, E. Lindahl, GROMACS 4: Algorithms for highly efficient, load-balanced, and scalable molecular simulation. *J. Chem. Theory Comput.* **4**, 435–447 (2008).
57. H. Fujitani, A. Matsuura, S. Sakai, H. Sato, Y. Tanida, High-level ab initio calculations to improve protein backbone dihedral parameters. *J. Chem. Theory Comput.* **5**, 1155–1165 (2009).

Acknowledgments: We thank A. Kimura (Department of Biological Sciences, Hokkaido University) for great support in observation of single kinesins using the TIRF microscopy.

Funding: This work was funded by Grants-in-Aid for Scientific Research on Innovative Areas "Molecular Robotics" JSPS KAKENHI grant JP24104004 (AK); Molecular Engine grant 18H05423, for Scientific Research (A) grant 18H03673, grant 21H04434 (A.K.); Grant-in-Aid for Challenging Research (Exploratory) grant 21K19877 (A.K.); Molecular Engine grant 18H05426 (M.I.); Program for Promoting Researches on the Supercomputer Fugaku grant JPMXP1020200201 and computational resources of the Fugaku computer and TSUBAME computer hp200129 and hp210172 (M.I. and T.Y.); Molecular Engine grant 19H05389, for Scientific Research (B) grant 18H01837 (T.U.); and NSF grant 1662329 (H.H.). **Author contributions:** Conceptualization: T.U., H.H., and A.K. Methodology: T.U., H.H., and A.K. Investigation: S.R.N., C.G., S.N., T.U., and A.K. (HS-AFM and TIRF observation); T.Y. and M.I. (MD simulation). Visualization: S.R.N., C.G., and S.N. Supervision: T.U., H.H., and A.K. Writing (original draft): S.R.N. and C.G. Writing (review and editing): S.R.N., C.G., A.M.R.K., K.S., T.Y., M.I., T.U., H.H., and A.K. **Competing interests:** The authors declare that they have no competing interests. **Data and materials availability:** All data needed to evaluate the conclusions in the paper are present in the paper and/or the Supplementary Materials.

Submitted 12 October 2020
Accepted 20 August 2021
Published 13 October 2021
10.1126/sciadv.abf2211

Citation: S. R. Nasrin, C. Ganser, S. Nishikawa, A. M. R. Kabir, K. Sada, T. Yamashita, M. Ikeguchi, T. Uchihashi, H. Hess, A. Kakugo, Deformation of microtubules regulates translocation dynamics of kinesin. *Sci. Adv.* **7**, eabf2211 (2021).

Deformation of microtubules regulates translocation dynamics of kinesin

Syeda Rubaiya NasrinChristian GanserSeiji NishikawaArif Md. RashedulKabirKazuki SadaTakefumi YamashitaMitsunori IkeguchiTakayuki UchihashiHenry HessAkira Kakugo

Sci. Adv., 7 (42), eabf2211. • DOI: 10.1126/sciadv.abf2211